https://doi.org/10.5194/amt-2023-150
Preprint. Discussion started: 24 July 2023

Atmospheric Measurement Techniques Discussions

Assessing the Ducting Phenomenon and its Impact on GNSS Radio Occultation Refractivity Retrievals over the Northeast Pacific Ocean using Radiosondes and Global Reanalysis

Thomas E. Winning Jr. [1], Feiqin Xie[1] and Kevin J. Nelson[1,a]
[1] Texas A&M University – Corpus Christi, Corpus Christi, 78412, USA
[a] now at: Jet Propulsion Laboratory, California Institute of Technology, Pasadena, 91109, USA
Correspondence to: Thomas E. Winning Jr. (twinning@islander.tamucc.edu)

Abstract. In this study, high-resolution radiosondes from the MAGIC field campaign and ERA5 global reanalysis data are used to assess the elevated ducting layer characteristics along the transect over the northeastern Pacific Ocean from Los Angeles, California to Honolulu, Hawaii. The height of the planetary boundary layer (PBLH) increases as the strength of the refractivity gradient and resultant ducting decrease from east to west across the analysis transect. The thickness of the ducting layer remains remarkably consistent (~110 m) in the radiosonde data. On the other hand, the ERA5 generally resolves the ducting features well but underestimates the ducting height and strength especially over the trade cumulus region near Hawaii. A simple two-step end-to-end simulation is used to evaluate the impact of the elevated ducting layer on RO refractivity retrievals. A systematic negative refractivity bias (N-bias) below the ducting layer is observed throughout the transect, peaking approximately 70 meters below the PBL height (−5.42%), and gradually decreasing towards the surface (−0.5%). Further, the underestimation of the N-bias in the ERA5 data increases in magnitude westward and while the correlation of the N-bias with the minimum gradient and sharpness are all strong; there is no evidence of zonal dependence.

1 Introduction

The troposphere, where most weather occurs, consists of two main layers: the planetary boundary layer (PBL) and the free atmosphere (FA) (Garratt, 1992). The PBL characteristics change frequently on both spatial and temporal scales and the PBL height (PBLH) can impact the exchange of heat, momentum, and particulate matter with the FA, making it a critical factor in global energy balances and water cycling (Stull 1988; Ramanathan et al. 1989; Klein and Hartmann 1993). Regular PBL observations are mainly limited to in situ measurements from

https://doi.org/10.5194/amt-2023-150
Preprint. Discussion started: 24 July 2023

Atmospheric Measurement Techniques Discussions

surface stations and radiosondes. However, spatially and temporally dense in situ PBL observations are only available from field campaigns such as the Boundary Layer Experiment 1996 (BLX96, Stull et al. 1997), the VAMOS Ocean-Cloud-Atmosphere-Land Study Regional Experiment (VOCALS-REx, Wood et al. 2011), and the Marine Atmospheric Radiation Measurement (ARM) GCSS Pacific Cross Section Intercomparison (GPCI) Investigation of Clouds (MAGIC, Zhou et al. 2015), etc. Satellite observations of the PBL are also limited due to signal attenuation of the conventional infrared sounder in the lower troposphere and the low vertical resolution of microwave sounding instruments. Additionally, while the depth of the PBLH can vary from a couple hundred meters to a few kilometers (von Engeln and Teixeira 2013; Ao et al. 2012), the transition layer from the PBL to the FA is typically on the order of tens to hundreds of meters thick (Maddy and Barnet 2008), rendering ineffective PBL sensing from the low vertical resolution passive infrared and microwave sounders.

On the other hand, Global Navigation Satellite System (GNSS) radio occultation (RO) provides global atmospheric soundings with a vertical resolution of approximately 100 m in the lower troposphere under all weather conditions (Kursinski et al. 1997, 2000). One of the major GNSS RO missions is the Formosat-3/Constellation Observing System for Meteorology, Ionosphere, and Climate (COSMIC), later referred to as COSMIC-1 (Anthes et al. 2008), and its follow-on mission COSMIC-2 (Schreiner et al. 2020). Numerous studies have documented the high value of GNSS RO for profiling the PBL and determining the PBLH (Nelson et al. 2021; Winning et al. 2017; Ao et al. 2012; ; Guo et al. 2011; Basha and Ratnam 2009; Ao et al. 2008; Xie et al. 2008).

The advancement of the GNSS RO technique with open-loop tracking (Sokolovskiy et al., 2006; Beyerle et al., 2003; Ao et al., 2003) along with the implementation of the radio-holographic retrieval algorithm (Jensen et al., 2004; Jensen et al., 2003; Gorbunov, 2002) have led to much improved PBL sounding quality. However, probing the marine PBL remains challenging as systematic negative biases are frequently seen in RO refractivity retrievals (Feng et al. 2020; Xie et al. 2010). One major cause of the refractivity bias (hereafter N-bias) is the RO retrieval error due to elevated atmospheric ducting often seen near the PBLH (Ao et al., 2007; Xie et al., 2006; Ao et al. 2003; Sokolovskiy 2003,). This elevated ducting prevails over the subtropical eastern oceans (von Englen et al., 2003; Lopez, 2009, Feng et al., 2020), and the horizontal extent of ducting in these regions can be on the order of thousands of kilometers (Winning et al. 2017; Xie

https://doi.org/10.5194/amt-2023-150
Preprint. Discussion started: 24 July 2023

Atmospheric Measurement Techniques
Discussions

et al. 2010). In the presence of ducting, the vertical refractivity gradient exceeds the critical refraction threshold for L-band frequencies (i.e., dN/dz ≤ −157 N-units km^{-1}). The steep negative refractivity gradient is often observed in the vicinity of the PBLH, which is typically caused by an atmospheric temperature inversion, a moisture lapse, or a combination of both. When ducting is present, the Abel inversion in the standard retrieval process encounters a non-unique inversion problem due to a singularity in the bending angle, resulting in large, systematic underestimation of refractivity (N) below the ducting layer (Sokolovskiy, 2003; Ao et al., 2003; Xie et al. 2006). The large uncertainty in RO refractivity coupled with the singularity in bending angle hinders assimilation of RO observations into numerical weather models, resulting in discarding of a significant percentage of RO measurements inside the PBL (Healy, 2001).

In order to thoroughly evaluate the N-bias attributed to ducting, the issue must be examined from the ground up by using a dense collection of observations where the occurrence of ducting in the lower troposphere is present in the daily climatology of the region. Section 2 provides details of the two data sets used for this study: high-resolution radiosondes over the northeastern Pacific Ocean and ERA5 reanalysis profiles colocated to the radiosondes. Additionally, we discuss the method used for colocation between the radiosondes and ERA5 profiles, as well as detection of the ducting layer and the corresponding PBLH. Section 3 presents the ducting climatology for key variables, such as ducting height, PBLH, minimum N-gradient, and gradient sharpness. The characteristics of ducting including the thickness and strength along the cross-section are also shown. Furthermore, we evaluate the ducting-induced N-bias in GNSS RO refractivity retrievals by carrying out a two-step end-to-end simulation. Section 4 summarizes the findings and discusses the direction of future research.

2 Data and methods

2.1 MAGIC radiosonde and colocated ERA5 data sets

A collection of high-resolution radiosondes from the Marine Atmospheric Radiation Measurement (ARM) GCSS Pacific Cross Section Intercomparison (GPCI) Investigation of Clouds (MAGIC) are utilized as the primary data set in this analysis (Lewis 2016; Zhou et al. 2015). The MAGIC field campaign took place from 26 September 2012 to 2 October 2013 as part of the U.S Department of Energy ARM Program Mobile Facility 2 (AMF2) aboard the

https://doi.org/10.5194/amt-2023-150
Preprint. Discussion started: 24 July 2023

Atmospheric Measurement Techniques Discussions
Open Access
EGU

Horizon Lines container ship, *Spirit*, which completed 20 round trip passes between Los Angeles, California and Honolulu, Hawaii during the yearlong data collection period (Painemal et al., 2015; Zhou, 2015). During each transit, radiosondes were launched at 6-hour intervals from the beginning of the program through the end of June 2013; the observation frequency increased to every 3 hours from July 2013 through the end of the campaign (Zhou et al., 2015). A total of 583 MAGIC radiosonde profiles were collected during the field campaign (Zhou et al., 2015), all with a vertical sampling frequency of 0.5 Hz (2 seconds), which provides an average vertical sampling interval of ~8 m below 3 km.

The number of observations and location (Fig. 1) of this data set serves multiple benefits. First, the northeast Pacific transitions from a shallow stratocumulus-topped PBL to a higher, trade-cumulus boundary layer regime along the GPCI transect (Garratt, 1992); this unique transition zone provides an ideal natural laboratory for studying the horizontal variation of the marine PBL. Second, the large number of observations over a 12-month time frame provides high temporal (diurnal and seasonal) and spatial profiling of the PBL along the GPCI transect. Finally, ducting is prevalent throughout the domain over which the observations were captured which creates an opportunity to perform an analysis over a natural cross-section of X (zonal) and Z (vertical) dimensions.

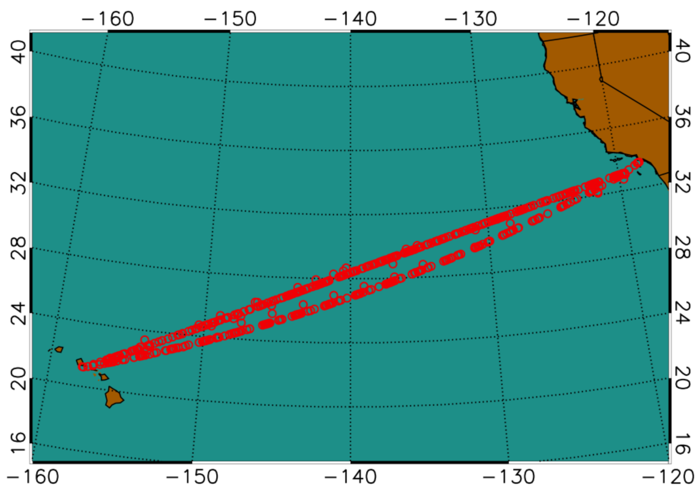

Figure 1: Location of radiosonde observations from the MAGIC field campaign October 2012–September 2013.

The radiosonde profiles are colocated with the ECMWF Reanalysis version 5 (ERA5, Hersbach et al. 2020). The ERA5 reanalysis data have a horizontal grid resolution of 0.25˚x0.25˚, 1-hour temporal resolution, and 137 vertical levels from the surface to 0.01 hPa (Hersbach et al., 2020).

https://doi.org/10.5194/amt-2023-150
Preprint. Discussion started: 24 July 2023

Atmospheric Measurement Techniques Discussions

An average of 19 model levels exist below 1 km providing the highest vertical resolution near the surface; vertical density of the model decreases with height to 8 levels within the 1 km–2 km layer and further decreasing to 5 levels within the 2 km–3 km. Each MAGIC radiosonde profile was colocated with the nearest ERA5 grid point that is within 1.5 hours of the closest 3-hourly model reanalysis profile.

2.2 PBL height detection with the minimum gradient method

At GNSS L-band frequencies, the atmospheric refractivity (*N* in N-units) is derived from the refractive index *n*, where $N= (n-1) \times 10^6$ and, in the neutral atmosphere (Kursinski et al., 1997), is a function of the atmospheric pressure (*P* in mb), temperature (*T* in K), and partial pressure of water vapor (P_w in mb) as seen in Eq. (1) from Smith and Weintraub (1953).

$$N = 77.6\frac{P}{T} + 3.73 \times 10^5 \frac{P_w}{T^2}, \quad (1)$$

Atmospheric refractivity decreases exponentially with height which, all else being equal yields a negative value vertical gradient. As such, the minimum refractivity describes the largest magnitude value.

Over the subtropical eastern oceans, a sharp decrease in moisture is often associated with a strong temperature inversion marking a clear transition from the PBL to the FA. Both the moisture lapse and the temperature inversion lead to a sharp negative refractivity gradient which can be precisely detected from GNSS RO. Numerous studies have implemented the simple minimum gradient method to detect the PBLH, which is the location of the minimum refractivity gradient (Ao et al., 2012; Seidal et al., 2010; Xie et al., 2006). When the vertical refractivity gradient is less than the critical refraction (dN/dz ≈ −157.0 N-units km^{-1}), ducting occurs (Sokolovskiy, 2003). To better assess the strength of the refractivity gradient for more robust PBLH detection with gradient method, Ao et al. (2012) introduced the sharpness parameter, which is defined as the ratio of the minimum vertical refractivity gradient to the root mean square error of the refractivity gradient profile (eq. 2).

$$\tilde{X}' \equiv -\frac{X'_{min}}{X'_{RMS}}, \quad (2)$$

Each refractivity gradient profile can then be filtered to identify the PBLH values with sharpness parameter exceeding a specific threshold, thus increasing the robustness of PBLH detection. In this study, the MAGIC radiosonde refractivity profiles were first interpolated to a uniform 10 m

https://doi.org/10.5194/amt-2023-150
Preprint. Discussion started: 24 July 2023

vertical grid and then smoothed by 100 m to reduce the noise in the N-gradient profile that is a result of the high sampling rate. Colocated ERA5 data were also vertically interpolated to the same 10 m grid but not smoothed as these data do not contain the inherent noise as the radiosonde observations.

2.3 Ducting layers

Instances of multiple ducting layers occurring within a profile are present for both the MAGIC (31.5%) and ERA5 (6.7%) data sets. A ducting layer is identified as any interval of continuous points with refractivity gradient equal to or less than −157 N-units km^{-1}. Note, however, we only refer to the "ducting layer" of each profile as the dominant ducting layer corresponding to the layer in which the minimum gradient is located (Fig. 2a–d). The ducting layer thickness (Δh) is defined as the interval between the top and bottom of the ducting layer where the N-gradients reach critical refraction. Similarly, the strength of each ducting layer (ΔN) is defined as the refractivity difference between the bottom and top of the ducting layer. The ducting layer height is in reference to the top of the ducting layer (Ao, 2007), which is generally slightly above the PBLH.

Figure 2 illustrates two ducting layers in a representative MAGIC radiosonde case near −150°, but only one in the colocated ERA5 profile. Profiles of radiosonde refractivity (N-units x 1/10, *N/10*), temperature (T) and specific humidity (q) and their respective gradients (dN/dz, dT/dz and dq/dz) are shown in Fig 2a and Fig. 2b, respectively. Similar plots for the collocated ERA5 profiles are shown in Fig. 2c and Fig. 2d. The PBLH of the radiosonde (2.10 km) is almost identical to the colocated ERA5 (2.14 km) and the "dominant" ducting layer near the PBLH demonstrates similar thickness. However, a second, weaker ducting layer seen in the radiosonde above the PBLH was not captured by the ERA5. This is likely due to the lower vertical resolution in ERA5 as can be seen in the gradient plots (Fig. 2b and Fig. 2d).

It is also worth noting that the residual layer between 1.2–1.5 km with gradient close to critical refraction is seen in the radiosonde is also seen in the ERA5 profile, but at a much lower altitude (~0.7 km).

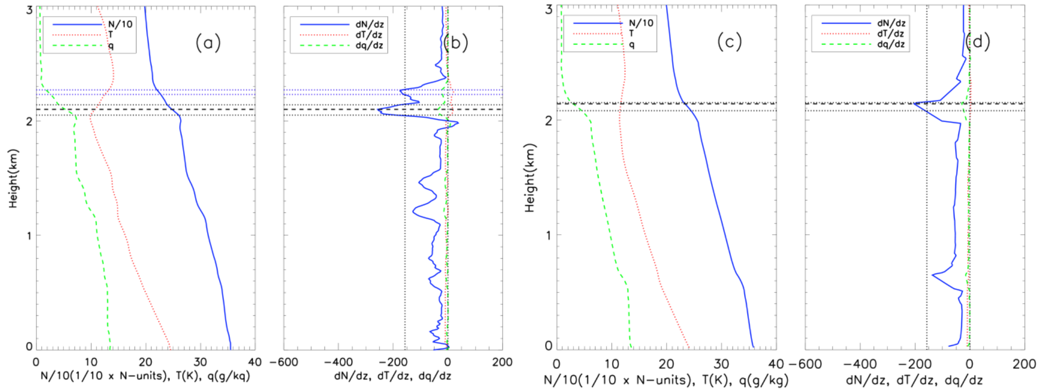

Figure 2: (a) MAGIC radiosonde (−150.00°) and (c) colocated ERA5 (−150.00°) profiles of refractivity (1/10 x N-units, *N/10*, solid blue), temperature (*T* in K, dotted red) and specific humidity (*q* in g kg^{-1}, dashed green); (b) the associated radiosonde and (d) ERA5 gradient profiles. The horizontal dashed line highlights the height of the minimum gradient, i.e., PBLH. The paired horizontal dotted lines represent the bottom and top of the two ducting layers in the radiosonde profile, but only one in the ERA5 profile.

2.4 Evaluation of GNSS RO N-bias resulting from ducting

In order to estimate the systematic negative N-bias in GNSS RO observations in the presence of ducting, we use an end-to-end simulation on the radiosonde and ERA5 refractivity profiles. The simulation consists of a two-step process adapted from Xie et al. (2006). The first step is to simulate the 1-dimentional GNSS RO bending angle as a function of impact parameter by forward Abel integration of an input refractivity profile assuming a spherically symmetric atmosphere. The second step is to simulate the GNSS RO refractivity retrieval by applying the Abel inversion on the simulated bending angle from step one. In the absence of ducting, the impact parameter (i.e., the product of refractive index and the radius of the curvature) decreases monotonically with height, allowing a unique solution to the inverse Abel retrieval. However, in the presence of an elevated ducting layer, the Abel retrieval systematically underestimates the refractivity profile due to the non-unique Abel inversion problem resulting from the singularity in bending angle across the ducting layer (Sokolovskiy 2003; Xie et al., 2006). It should be noted that an additional 50 m vertical smoothing has been applied to the simulated bending angle profiles of both radiosonde and ERA5 data sets to alleviate the challenge of integration through the very sharp bending angle resulting from ducting in the inverse Abel integration procedure (Feng et al., 2020).

Figure 3 shows the end-to-end simulation results for the same radiosonde (a–d) and the colocated ERA5 (e–h) cases from Fig. 2. Figures 3a and 3e show the input refractivity profile (N_{rds} and

https://doi.org/10.5194/amt-2023-150
Preprint. Discussion started: 24 July 2023

N_{ERA5}) and corresponding Abel refractivity retrieval (N_{Abel}), respectively. The PBLH is marked by a horizontal dotted line. The peak bending angle is consistent with the sharp refractivity gradient. Figure 3b shows the fractional N-bias between the simulated Abel retrieved RO refractivity profile and the observation, i.e., $((N_{Abel} - N_{Obs})/N_{Obs})$. Considering the significant spatial and temporal variations of ducting height along the transect, each N-bias profile is normalized to its PBLH for the purposes of comparison. For example, the zero-adjusted height refers to the PBLH for each individual profile. The systematic negative N-bias is clearly shown below the ducting layer marked by the PBLH in both cases, with the biases decreasing at lower altitude, the largest magnitude bias (−5% for radiosonde; −2.5% for ERA5) close to the ducting height and a minimum magnitude approaching zero near the surface.

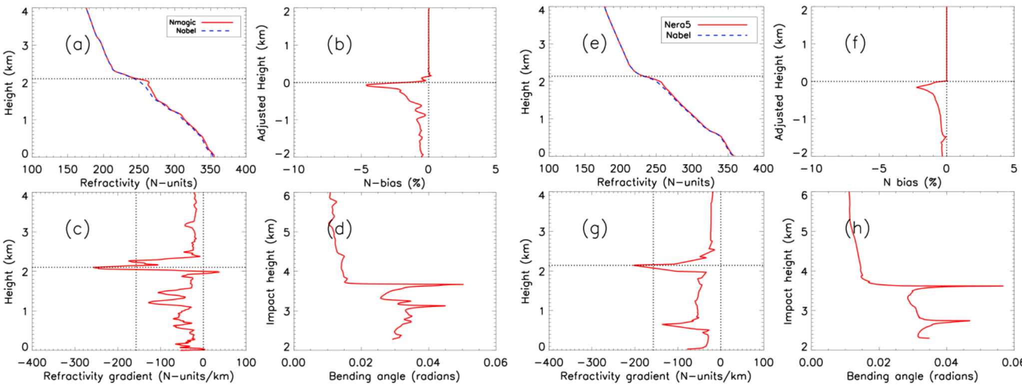

Figure 3: Four-panel comparison of individual profiles of N_{Obs} vs. N_{Abel} that are reconstructed through the end-to-end simulation. Four-panels for MAGIC of: (a) N_{Obs} (solid red) and N_{Abel} (blue dashed) from surface to 10 km; (b) adjusted N-bias $((N_{Abel} - N_{Obs})/ N_{Obs})$; (c) minimum gradient and (d) bending angle vs. impact parameter. Colocated ERA5 profiles are shown in panels e-h, respectively.

3 Analysis

Out of a total of 583 MAGIC radiosonde (and co-located ERA5) profiles, quality control has been implemented based on five key criteria. First, a total of 19 radiosonde and 24 ERA5 profiles near the southern California coast were removed due to a zonal position east of −120° or anomalously high PBL heights (PBLH > 3.0 km) with no distinct minimum gradient. The remaining profiles in the easternmost portion of the domain were too few in number to calculate meaningful statistics. Second, any profile lacking critical refraction (i.e. $dN/dz < -157$ N-units km^{-1}) points was excluded from the analysis which resulted in the removal of 47 radiosonde and 176 ERA5 profiles. Third, the noisy bending angle could result in errors in Abel refractivity retrieval and cause positive N-bias. Therefore the profiles with N-bias greater than +0.5% are excluded resulting in the removal of 61 MAGIC profiles and 16 ERA5 profiles. Fourth, the profiles with only surface ducting are discarded when the only refractivity gradient less than −157 N-units km^{-1} occurs below the 300 m threshold. Finally, 25 radiosonde profiles and 2 ERA5 profiles were removed due to the Abel retrieval failure. After implementing all quality control measures, the number of radiosonde and ERA5 profiles used for the N-bias analysis is reduced to 396 and 319 profiles, respectively.

3.1 PBL climatology

To evaluate the ducting climatology along the transect from the coast of southern California to Hawaii, we group the MAGIC radiosonde and the colocated ERA5 profiles into eight 5° longitude bins between −160.0° and −120.0°. The equally spaced bins are centered at −157.5°, −152.5°, −147.5°, −142.5°, −137.5°, −132.5°, −127.5° and −122.5° which allows for the spatial variation of the PBL, ducting layer and the associated properties along the transect to be easily illustrated. Figure 4 shows the median value of PBLH (a), sharpness (b) and minimum gradient (c) along the transect. The median-absolute-deviation (MAD) for each parameter is also shown.

In Fig. 4a, the MAGIC radiosondes clearly show the gradual increase of the PBLH along the transect from the shallow stratocumulus-topped PBL (~800 m) near the southern California coast westward to the much deeper trade-cumulus regime (~1.8 km) near Hawaii. A similar structure is seen in the colocated ERA5 data but with an average low bias of 165 m below the radiosonde. However, a nearly 800 m underestimation in PBLH over the two westernmost bins near Hawaii is also seen, this is consistent with what is found over the equivalent trade cumulus region of the subtropical southeast Pacific Ocean (Xie et al., 2012). Such a discrepancy could be due to the decreasing vertical resolution with height in the ERA5 profiles. This results in a sharper refractivity gradient caused by the frequent residual layer (below 1 km) as compared to the actual PBLH near 2 km. Note that the larger median absolute deviation for the westernmost bins compared to the rest of the transect illustrates the existence of greater PBLH variability closer to the trade-cumulus boundary layer regime.

The westward decreasing magnitude of the minimum refractivity gradient (Fig. 4b) and sharpness parameter (Fig. 4c) indicates the westward weakening of moisture lapse and/or

https://doi.org/10.5194/amt-2023-150
Preprint. Discussion started: 24 July 2023

Atmospheric Measurement Techniques
Discussions

temperature inversion across the PBL top, which is consistent with the decreasing synoptic-scale subsidence from the California coast to Hawaii.

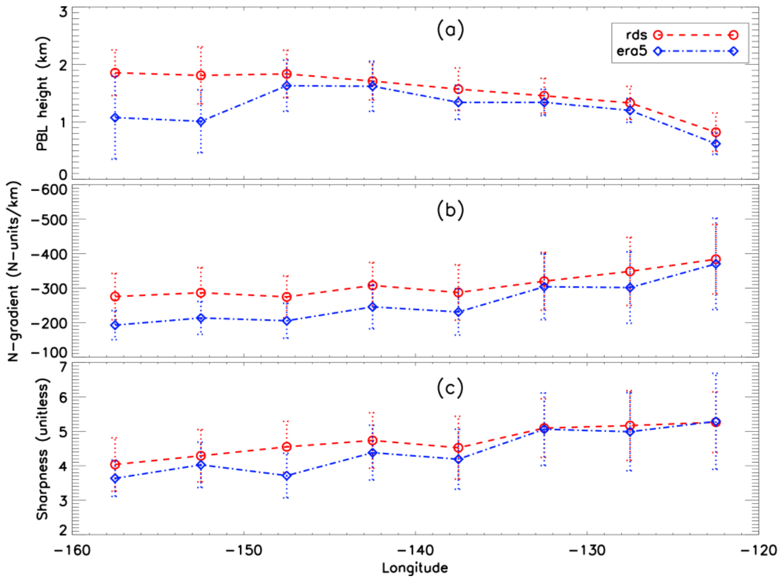

Figure 4: Zonal transect of 5° bin MAGIC and ERA5 (a) PBLH, (b) sharpness parameter and (c) minimum refractivity gradient for MAGIC (median in red circle, MAD in dashed error bars) and ERA5 (median in blue diamond, MAD in dot-dashed error bars).

It is also notable that the ERA5 systematically underestimates not only the PBLH, but also the magnitude of the minimum N-gradient across the entire transect; this can also be seen in the sharpness parameter west of −132.5°. This discrepancy could again be partially attributed to the decrease in vertical sampling in ERA5 profiles as compared to the radiosondes, the result of which leads to a weaker PBL N-gradient and coincides with an increasing PBLH. Therefore, the underestimation of the ERA5 minimum N-gradient increases in magnitude from east to west and becomes most prominent near Hawaii where the PBLH reaches the maximum height over the region.

3.2 Ducting climatology

As introduced in Sect. 2.3, the key characteristics of the ducting layer along the transect will be investigated, these include the ducting layer height, thickness (Δh), and strength (ΔN), as well as the average refractivity gradient within the ducting layer ($\Delta N/\Delta h$).

https://doi.org/10.5194/amt-2023-150
Preprint. Discussion started: 24 July 2023

Atmospheric Measurement Techniques Discussions

The ducting layer heights from both radiosonde and ERA5 show a westward increase along the transect (Fig. 5a), which is similar to the PBLH in Fig. 4a. Note again that the ERA5 shows a systematic ~100–200 m low bias when compared to the radiosondes between −122.5˚ and −147.5˚, with the difference increasing to more than 500 m near Hawaii.

The ducting layer thickness is the median height from the bottom of the ducting layer to the top and is expressed in km (Fig. 5b). Ducting thickness (Δh) for MAGIC shows a near constant value of 110 m across the entire transect with only a slight increase to 130 m at −122.5˚; this is consistent with findings from Ao et al. (2003). Conversely, the ERA5 shows a constant but slightly thicker ducting layer to the east of −137.5˚ and then a decreasing thickness to the west of −137.5˚ (Fig. 5b).

The ducting layer strength is the decrease in refractivity from the bottom of the ducting layer to the top (Fig. 5c) and the ratio $\Delta N/\Delta h$ reflects the average gradient of the ducting layer (Fig. 5d). The ducting strength (ΔN) for the radiosondes ranges from 25 N-units near Hawaii to 40 N-units near the coast of California. Both ΔN and $\Delta N/\Delta h$ show an overall westward decreasing trend along the transect which is consistent with the decrease in magnitude of the N-gradient (Fig. 4b). Note that MAGIC and ERA5 show similar ducting strength in the eastern part of the region but diverge near −137.5˚ with ERA5 10 to 20 N-units weaker than the MAGIC profiles. On the other hand, ERA5 shows a systematic lower average refractivity gradient ($\Delta N/\Delta h$) than MAGIC throughout the transect, indicating the challenge in ERA5 to consistently resolve the sharp vertical structure in refractivity, and likewise in temperature and moisture profiles, across such a thin ducting layer. The problem becomes acutely clear near the trade cumulus region.

https://doi.org/10.5194/amt-2023-150
Preprint. Discussion started: 24 July 2023

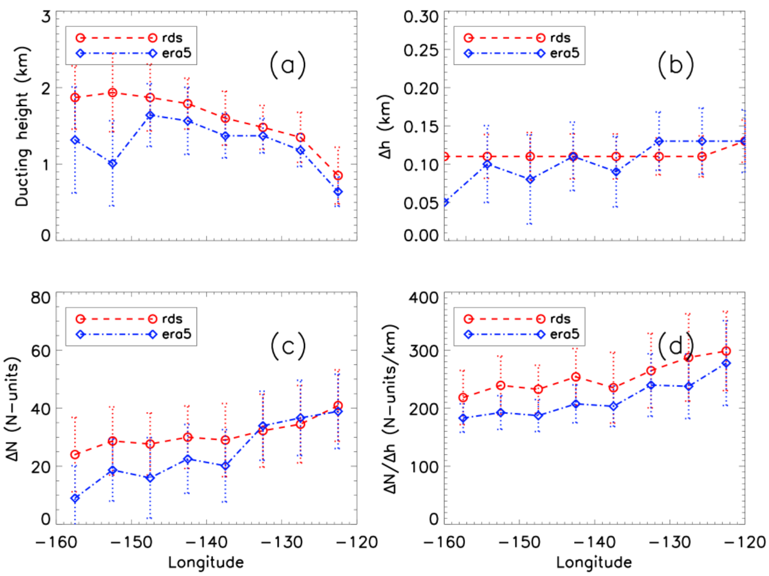

Figure 5: Zonal transect of 5° bin median (a) ducting height, (b) ducting layer thickness (Δ*h*), (c) ducting layer strength (Δ*N*), and (d) average ducting layer gradient Δ*N*/Δ*h* for MAGIC (median in red circle and red-dashed line, MAD in red-dotted error bars) and ERA5 (median in blue diamond and dot-dashed error bars, MAD in blue-dotted error bar).

Figure 6 shows ducting layer thickness as a function of ducting layer strength, with each data point colored by its respective longitude bin. The relationship between Δ*h* and Δ*N* is not longitude-dependent for either data set, but a linear trend is evident for thinner ducting layers (Δ*h* < 0.1 km) with weaker ducting strength (Δ*N* < ~25 N-units). However, for the ducting layers thicker than the median value of 0.1 km, such a trend becomes less identifiable, and the ducting strength Δ*N* begins to show more variability toward larger values.

https://doi.org/10.5194/amt-2023-150
Preprint. Discussion started: 24 July 2023

Atmospheric Measurement Techniques Discussions

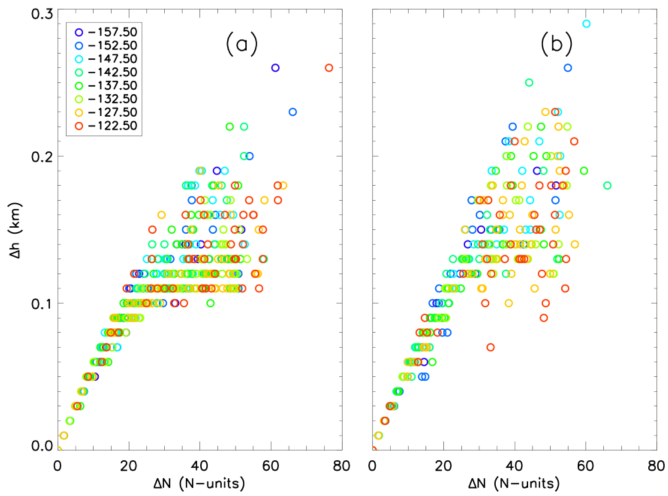

Figure 6: Comparison of individual profiles' ducting strength (Δ*N*) vs. ducting thickness (Δ*h*) for MAGIC (a) and ERA5 (b). The color of each circle represents the location of the 5° longitude bin of each observation.

3.3 Ducting-induced GNSS RO N-bias statistics

To estimate the systematic negative N-bias in GNSS RO observations due to ducting, we have applied the end-to-end simulation to all radiosonde and ERA5 refractivity profiles with at least one elevated ducting layer detected (details in Sect. 2.5). The N-bias climatology along the transect as well as its relationship to the ducting properties are presented below.

3.3.1 N-bias climatology

Figure 7 shows a composite of both MAGIC (396 profiles) and ERA5 (319 profiles) N-bias profiles which have been normalized to their PBLH, with the median N-bias and MAD overlaid. The comparison reveals a number of occurrences of multiple ducting layers above the minimum gradient identified PBL in the MAGIC data while there are significantly less occurrences in the ERA5 data. Figure 7 illustrates the systematically negative N-bias peaks at nearly 100 m below the PBLH (ducting height) and decreases at lower altitudes. Many radiosonde profiles show smaller negative N-biases above the PBLH (e.g., zero adjusted height), but only a few in ERA5 which is a result of the secondary ducting layers above the major ducting layer near PBLH. The peak median value of the N-bias for radiosondes is −5.42% (MAD, 2.92%), nearly twice the ERA5 value of −2.96% (MAD, 2.59%). It is worth noting that the variabilities (MAD) between the radiosonde and ERA5 data are very close to each other.

https://doi.org/10.5194/amt-2023-150
Preprint. Discussion started: 24 July 2023

Atmospheric Measurement Techniques
Discussions

A closer look at each data set reveals that the difference between the 5˚median PBLH and height of the maximum N-bias ($h_{PBL} - h_{N\text{-bias}}$) is positive for all bins. The maximum difference of 100 m is located in bin −137.5˚ and a minimum difference of ~15 m at bin −152.5˚. Comparatively, the ERA5 reflects a PBL height greater than the N-bias height for each bin with a maximum difference of 230 m located at −142.5˚ and a minimum of ~45 m at −157.5˚. The ERA5 data show a larger average height difference between the PBL and N-bias (120 m) than the radiosonde data (70 m).

The N-bias comparison of the 5˚ bin median values of the two data sets favors the radiosonde data with smallest magnitude difference located at bin −147.5˚ (−4.37%) and largest magnitude difference of −7.86% located at bin −122.5˚. Comparatively, the ERA5 minimum N-bias difference of −0.77% −157.5˚) is much lower than the radiosonde while the maximum difference is similar in both magnitude −5.92%) and location (−122.5˚).

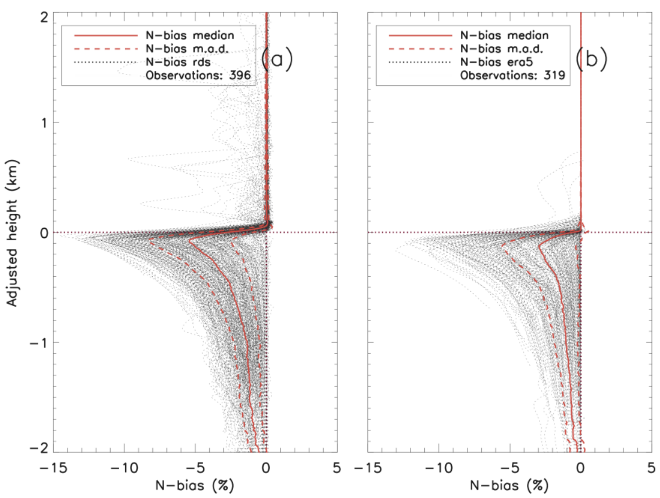

Figure 7: Fractional refractivity difference (N-bias) between the simulated Abel-retrieved refractivity profile and the original observation profile (($(N_{Abel} - N_{Obs})/N_{Obs}$), for all individual observations (dotted gray): (a) MAGIC radiosondes (396 total profiles) and (b) ERA5 (319 total profiles) with population median (solid red) ± MAD (dashed red). Note the zero value in the adjusted height refers to the PBLH for each individual N-bias profile.

3.3.2 N-bias along the transect

To illustrate the large variation in the N-bias vertical structure resulting from the spatial variation of ducting height and strength, we separately present the N-bias profiles (median ± MAD) for each 5˚ bin, replacing the zero adjusted height with the median PBLH for each bin (Fig. 8). The radiosonde composite (Fig. 8a) illustrates the transition of the median N-bias height from 1.8 km

https://doi.org/10.5194/amt-2023-150
Preprint. Discussion started: 24 July 2023

at Honolulu, HI to 0.8 km near the coast of Los Angeles, CA. Table 1 provides supplemental values for the Fig. 8 illustration of the radiosonde and ERA5 statistical climatology. The radiosonde N-bias variation shows a minimum magnitude of near the center of the transect and two of the largest magnitude difference values of as the bookends while the ERA5 N-bias values have a larger range but peak values (−5.41% to −6.23%) in the three bins closest to California; note the significantly reduced peak N-bias to the west of −137.5˚ (−3.10% to −0.71%). Moreover, a discontinuity exists in the two westernmost longitude bins (−157.5˚ and −152.5˚) which show a markedly lower and weaker N-bias.

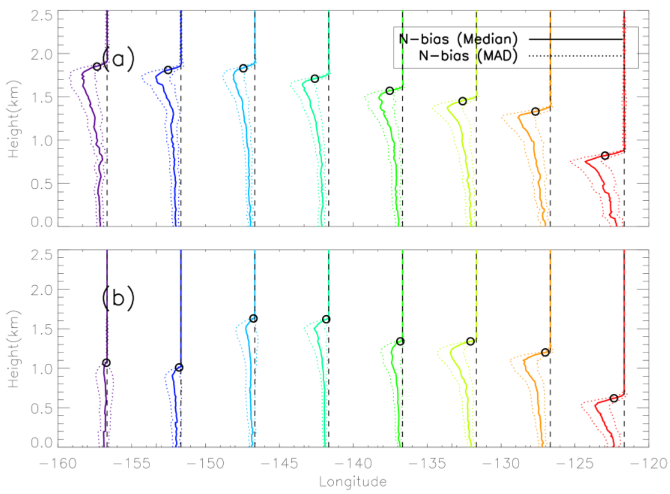

Figure 8: Median N-bias (solid) ± MAD (dotted) along the north Pacific transect for MAGIC radiosondes (a) and ERA5 (b). Open circles represent the median PBL height for each 5˚ bin.

Table 1: 5˚ bin median and MAD peak N-bias values for MAGIC radiosondes (RDS) and ERA5.

Peak N-bias				
Longitude	RDS median	RDS MAD	ERA5 median	ERA5 MAD
-157.5˚	-6.11	±2.85	-0.71	±1.80
-152.5˚	-5.24	±2.91	-2.23	±1.68
-147.5˚	-4.85	±2.18	-2.03	±2.25
-142.5˚	-5.78	±2.44	-3.10	±2.24
-137.5˚	-5.34	±2.95	-2.60	±2.21
-132.5˚	-5.92	±3.14	-5.41	±2.79
-127.5˚	-6.42	±3.38	-5.60	±2.74
-122.5˚	-8.10	±3.27	-6.23	±2.98

https://doi.org/10.5194/amt-2023-150
Preprint. Discussion started: 24 July 2023

Figure 9 further illustrates the peak N-bias, median PBL N-bias and the near surface N-bias (at 0.3 km) at each bin along the transect. Note that the quality control process removes the refractivity profiles below 0.3 km. Therefore, the median N-bias is the median value from the near surface (0.3 km) to the PBLH.

Contrary to the general trend of westward decrease in magnitude of the minimum N-gradient (Fig. 4b) and ducting strength (Fig. 5c), the radiosonde peak N-bias shows the maximum (median: −8.10%, MAD: 3.26%) near California (−122.5˚) and the minimum (median: −4.85%, MAD: 2.18%) over the transition region (−147.5˚) as well as a slight increase to a secondary maximum (median: −6.11%, MAD: 2.85%) near Hawaii (−157.5˚). The median PBL N-bias and the near surface N-bias also show a similar pattern. However, the median N-bias demonstrates a sharp decrease in the eastern half of the domain from −5.25% (MAD: 2.71%) at −122.5˚ to −1.71% (MAD: 1.26%) at −137.5˚, and then remains relatively constant over the western half of the domain. Similarly, the near surface N-bias reaches a maximum magnitude of −3.54% (MAD: 2.11%) and sharply decreases to −1.06% (MAD: 0.85%) at −137.5˚, and then remains relatively constant over the western half of the domain.

It is important to point out that the much higher ducting height and larger variation near Hawaii as compared to California leads to smoothed and much smaller median N-gradient values (Fig. 4b), which also results in a smaller N-bias without being normalized to the PBLH. Therefore, the normalized N-bias observed near Hawaii indicates the presence of strong ducting over the trade-cumulus boundary layer regime (Fig. 8a), which will lead to comparable N-bias to that over the stratocumulus topped PBL.

On the other hand, the ERA5 data show a westward decrease of all three N-biases, systematically underestimating all three as compared to the radiosondes. This is expected as the decrease of ERA5 vertical resolution at higher altitude leads to a weaker PBL N-gradient observation (Fig. 4b), and thus weaker ducting and a smaller ducting-induced N-bias. Such underestimation of the N-bias in the ERA5 is at a minimum near California where the PBLH is lowest but becomes more severe westward with an increase in height, reaching a maximum magnitude N-bias difference near Hawaii. In this case, the peak N-bias is merely −0.71% (MAD: 1.80%) as compared to −6.23% (MAD: 2.98%) at −122.5˚ (Fig. 9a and Table 1). The large difference seen in the N-bias along the transect strongly indicates the challenges of the ERA5 data to resolve the sharp gradient across the ducting layer, resulting in a large variation in PBLH of the ERA5 data

https://doi.org/10.5194/amt-2023-150
Preprint. Discussion started: 24 July 2023

in the western segment of the region. The increasing difference between the radiosonde and ERA5 data from east to west is most pronounced in the peak N-bias cross-section (Fig. 9a) but is also clearly evident in both the median N-bias (Fig. 9b) as well as the near surface N-bias (Fig. 9c).

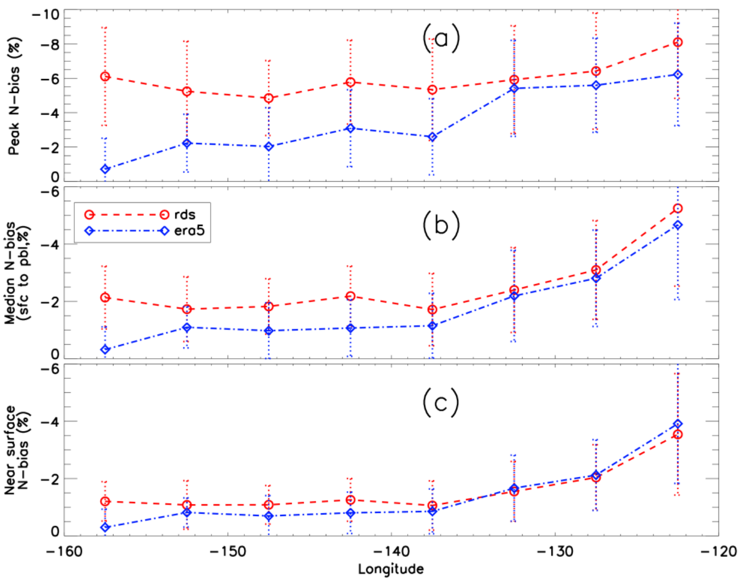

Figure 9: Zonal transect of 5° bin (a) peak N-bias, (b) median PBL N-bias, and (c) near surface N-bias at 0.3 km for MAGIC (median in red circle and red-dashed line, MAD in red-dotted error bar) and ERA5 (median in blue diamond and dot-dashed line, MAD in blue-dotted error bar)

3.3.3 N-bias climatology and key variable analysis

Figure 10 shows a scatter plot of the PBLH vs. height of maximum N-bias along the transect with each data point colored by the center longitude of the bin to which it belongs. The PBLH and the height of maximum N-bias show a clear linear relationship with high correlation for both the MAGIC (0.89) and ERA5 (0.98) data. The majority of the radiosonde data show the heights of the maximum N-bias aligns well with the PBLH but with a very small low bias (less than 70 m). The reason for the lower correlation value when compared to the ERA5 data is attributed to the radiosonde N-bias profiles with a double peak at which the larger magnitude bias is located (Fig. 7a). On the other hand, the ERA5 maximum ducting heights show little difference from the PBLH near California (e.g., −122.5°), but become lower moving westward, which is illustrated by the increasing difference between the linear regression line and the 1:1 line.

https://doi.org/10.5194/amt-2023-150
Preprint. Discussion started: 24 July 2023

Atmospheric Measurement Techniques Discussions

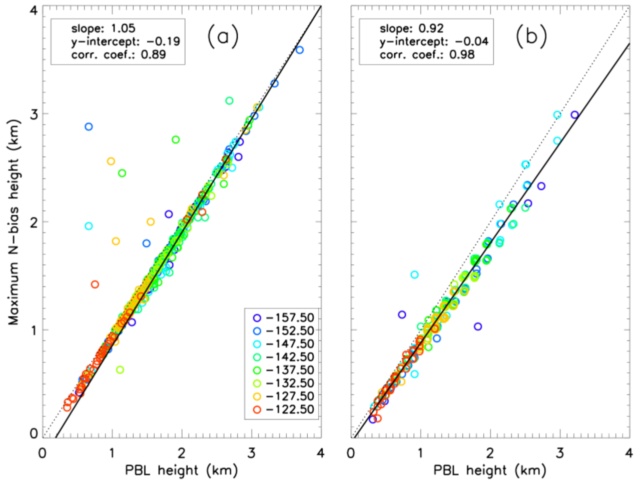

Figure 10: PBLH vs. height of maximum N-bias for individual profiles from MAGIC (a) and ERA5 (b) data. The color of each open circle represents the center longitude of the 5° bin to which each profile belongs.

Figure 11 shows the minimum refractivity gradient as a function of ducting-induced refractivity bias for MAGIC radiosondes (a) and ERA5 (b) and the corresponding sharpness parameters (c) and (d), respectively. A near-linear relationship between the minimum refractivity gradients and the maximum N-biases is evident for both MAGIC radiosondes and ERA5 profiles; in other words, the sharper the N-gradient, the larger the N-bias. The linear fit function along with the correlation coefficient for both MAGIC radiosondes (0.93) and the ERA5 profiles (0.88) are also presented.

The sharpness parameter (Fig. 11c, 11d) also shows a linear relationship with the maximum N-bias which is a result of its dependence on the minimum N-gradient. While a similar conclusion can be reached, it is interesting to note that the difference in the correlation of the radiosonde (−0.83) and the ERA5 (−0.84) does not lie in the observations with the larger magnitude peak N-bias, but in those closer to zero as the radiosonde data clearly centers below the regression line and trends above while the ERA5 with peak N-bias less than 5% are centered around the regression line. In the case of both key variables, their relationship with the peak N-bias exhibits no indication of zonal dependence.

https://doi.org/10.5194/amt-2023-150
Preprint. Discussion started: 24 July 2023

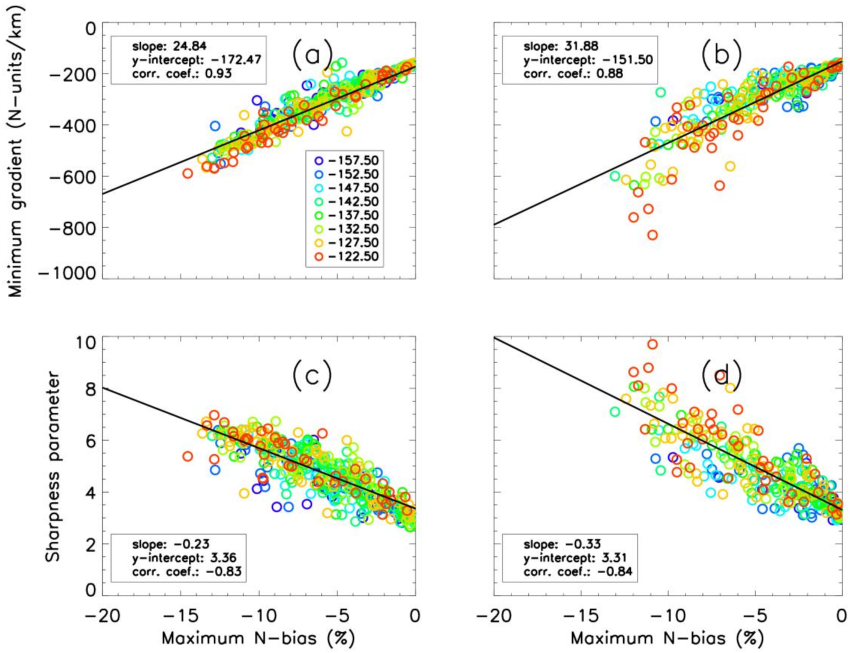

Figure 11: (a, b) Minimum refractivity gradient (N-units km^{-1}) and (c, d) sharpness parameter, as a function of the maximum N-bias (%) for MAGIC (a, c) and ERA5 (b, d) data with the line of linear regression in solid black. Color of each open circle represents the center longitude of the 5° bin to which each profile belongs.

4 Summary and Conclusions

In this study, radiosonde profiles from the MAGIC field campaign have been analyzed to investigate the ducting climatology and the impact of associated systematic refractivity biases that occur over the eastern North Pacific Ocean between Hawaii and California. Colocated ERA5 reanalysis data were used as a secondary comparison to the radiosonde observations.

The nearly 1-year high-resolution MAGIC radiosonde dataset reveals the frequent presence of ducting at a well-defined PBL throughout the transect marked by a sharp refractivity gradient resulting from the large moisture lapse across a strong temperature inversion layer. The PBLH increases by more than 1 km along the transect from CA to HI while the magnitude of the N-gradient decreases by 100 N-units km^{-1}. The zonal gradient of both variables illustrates the transition of the PBL from shallow stratocumulus adjacent to the California coast to deeper trade-wind cumulus that are prevalent near the Hawaiian Islands.

To estimate the systematic negative N-bias in GNSS RO observations due to ducting, we applied an end-to-end simulation on all radiosonde refractivity profiles that contained at least one

https://doi.org/10.5194/amt-2023-150
Preprint. Discussion started: 24 July 2023

elevated ducting layer. The ducting layer thickness remained remarkably consistent (110 m) across the transect with westward decreasing strength and increasing height. The ERA5 slightly underestimates both the height and strength of the ducting layer and so the PBLH.

The maximum N-bias occurs just below the PBLH, where the refractivity gradient is strongest. The height of the maximum N-bias and the PBLH show a highly positive correlation. The mean difference between the two is about 70 meters in the radiosonde but increasing to about 120 meters in the colocated ERA5 data. The correlation between the PBLH and the height of the maximum N-bias is highly positive.

MAGIC radiosondes indicated larger values of both ducting strength (ΔN) and thickness (Δh) than from ERA5 in the western half of the transect. The reverse is true in the eastern portion of the domain, and is likely associated with the transition of the cloud layer from open-cell cumulus in the west to stratocumulus and stratus in the east (Wood et al., 2011; Bretherton et al., 2019). While this segment of the transect also coincides with a better sampling rate for the ERA5 data (~40 m vertical resolution), the ERA5 continues to systematically underestimate the average ducting layer gradient climatology ($\Delta N/\Delta h$) when compared to the radiosondes. The largest N-bias is located in the region of strongest ducting which also corresponds to the largest sharpness parameter. The limited number of model levels in ERA5 near 2 km causes ducting to be underrepresented near the trade wind inversion which is evident in the discrepancy between the radiosonde and ERA5 PBLH cross sections.

Future work will include a comprehensive simulation study to explore the regional difference in horizontal inhomogeneity and its impact on GNSS RO soundings. This research will improve RO data quality, enhance understanding of PBL inhomogeneity, and advances weather and climate prediction capabilities.

https://doi.org/10.5194/amt-2023-150
Preprint. Discussion started: 24 July 2023

5 Data availability

Data for the Marine Atmospheric Radiation Measurement (ARM) GCSS Pacific Cross Section Intercomparison (GPCI) Investigation of Clouds (MAGIC, Zhou et al., 2015) can be accessed through the U.S. Department of Energy's Office of Science https://www.arm.gov/research/campaigns/amf2012magic.
Data for the ECMWF Reanalysis version 5 (ERA5, Hersbach et al., 2020) can be accessed at https://www.ecmwf.int/en/forecasts/dataset/ecmwf-reanalysis-v5.

6 Author contribution

Author Thomas Winning is responsible for all original text and, data analysis and production of graphics. Author Kevin Nelson contributed by providing updated data processing code, colocation of ERA5 data with MAGIC observations and first and second round edits. Author Feiqin Xie is the academic advisor for the primary author and also provided draft edits and paper organization and writing guidance.

7 Acknowledgements

The authors acknowledge funding support of earlier work from NASA grant (NNX15AQ17G). Authors T. Winning and K. Nelson were also partially supported by research assistantship from Coastal Marine System Science Program at Texas A&M University – Corpus Christi. The high-resolution ERA5 reanalysis data were acquired from ECMWF. The MAGIC radiosonde data were provided by the Atmospheric Radiation Measurement program (ARM) Climate Research Facility sponsored by the U.S. Department of Energy (DOE).
Author T. Winning's current affiliation: Ventura County Air Pollution Control District, Ventura, CA, 93003, USA. Author T. Winning acknowledges this work was done as an academic pursuit in association with Texas A&M University – Corpus Christi and not in the author's capacity as an employee of the Ventura County Air Pollution Control District.
Author K. Nelson's current affiliation: Jet Propulsion Laboratory, California Institute of Technology, Pasadena, 91109, USA. Author K. Nelson acknowledges this work was done as a private venture and not in the author's capacity as an employee of the Jet Propulsion Laboratory, California Institute of Technology.

References

Anthes, R. A., and Coauthors: The COSMIC/FORMOSAT-3 Mission: Early Results, BAMS, 89, 313–334, doi.org/10.1175/bams-89-3-313, 2008.

Ao, C. O., Meehan T. K., Hajj, G. A., Mannucci, A. J., and Beyerle, G.: Lower Troposphere Refractivity Bias in GPS Occultation Retrievals, J. Geophys. Res., 108, 4577, doi:10.1029/2002JD003216, 2003.

Ao, C. O.: Effect of Ducting on Radio Occultation Measurements: An Assessment Based on High-resolution Radiosonde Soundings, Radio Sci., 42, RS2008, doi.org/10.1029/2006RS003485, 2007.

Ao, C. O., Chan, T. K., Iijima, A., Li, J.-L., Mannucci, A. J., Teixeira, J., Tian, B., and Waliser, D. E.: Planetary Boundary Layer Information from GPS Radio Occultation Measurements, in: Proceedings of the GRAS SAF Workshop on Applications of GPSRO Measurements, Vol. 5 of, GRAS SAF Workshop on Applications of GPSRO Measurements, Reading, United Kingdom, ECMWF and EUMETSAT, 123–131, https://www.ecmwf.int/sites/default/files/elibrary/2008/7459-planetary-boundary-layer-information-gps-radio-occultation-measurements.pdf, 16–18 June, 2008.

Ao, C. O., Waliser, D. E., Chan, S. K., Li, J.-L., Tian, B., Xie, F., and Mannucci, A. J.: Planetary boundary layer heights from GPS radio occultation refractivity and humidity profiles, J. Geophys. Res., 117, D16117, doi:10.1029/2012JD017598, 2012.

Basha, G., and Ratnam, M. V.: Identification of atmospheric boundary layer height over a tropical station using high-resolution radiosonde refractivity profiles: Comparison with GPS radio occultation measurements, J. Geophys. Res., 114, doi.org/10.1029/2008jd011692, 2009.

Beyerle, G., Gorbunov, M. E., and Ao, C.O.: Simulation studies of GPS radio occultation measurements, Radio Sci., 38, 1084, doi:10.1029/2002RS002800, 2003.

Bretherton, C.S., and Coauthors: Cloud, Aerosol, and Boundary Layer Structure across the Northeast Pacific Stratocumulus–Cumulus Transition as Observed during CSET, Mon.Wea. Rev., 147, 2083–2102. DOI: 10.1175/MWR-D-18-0281, 2019

Feng, X., Xie, F., Ao, C.O., and Anthes, R.A.: Ducting and Biases of GPS Radio Occultation Bending Angle and Refractivity in the Moist Lower Troposphere, J. Atmos. Oceanic Technol., 37, 1013–1025, doi.org/10.1175/HTECH-D-19-0206.1, 2020.

Garratt, J. R.: Review: the atmospheric boundary layer, Earth-Sci. Rev., 37, 89–134, 1994

https://doi.org/10.5194/amt-2023-150
Preprint. Discussion started: 24 July 2023

Atmospheric Measurement Techniques
Discussions

Guo, P., Kuo, Y. H., Sokolovskiy, S. V., and Lenschow, D. H.: Estimating Atmospheric Boundary Layer Depth Using COSMIC Radio Occultation Data, J. Atmos. Sci., 68, 1703–1713, doi.org/10.1175/2011jas3612.1, 2011.

Gorbunov, M. E.: Canonical transform method for processing radio occultation data in the lower troposphere, Radio Sci., 37(5), 1076, doi:10.1029/2000RS002592, 2002.

Healy, S. B.: Radio occultation bending angle and impact parameter errors caused by horizontal refractive index gradients in the troposphere: A simulation study, J. Geophys. Res, 106, D11, 11875–11889, doi:10.1029/2001JD900050, 2001.

Hersbach, H., Bell, B., Berrisford, P., Hirahara, S., Horányi, A., Muñoz-Sabater, J., Nicolas, J., Peubey, C., Radu, R., Schepers, D., Simmons, A., Soci, C., Abdalla, S., Abellan, X., Balsamo, G., Bechtold, P., Biavati, G., Bidlot, J., Bonavita, M., De Chiara, G., Dahlgren, P., Dee, D., Diamantakis, M., Dragani, R., Flemming, J., Forbes, R., Fuentes, M., Geer, A., Haimberger, L., Healy, S., Hogan, R. J., Hólm, E., Janisková, M., Keeley, S., Laloyaux, P., Lopez, P., Lupu, C., Radnoti, G., de Rosnay, P., Rozum, I., Vamborg, F., Villaume, S., and Thépaut, J.-N.: The ERA5 Global Reanalysis, Q. J. Roy. Meteor. Soc., 146, 1999–2049, https://doi.org/10.1002/qj.3803, 2020.

Jensen, A. S., Lohmann, M.S., Nielsen, A.S. and Benzon, H.-H.: Geometrical optics phase matching of radio occultation signals, Radio Sci., 39, RS3009, doi:10.1029/2003RS002899, 2004.

Jensen, A. S., Lohmann, M.S., Benzon, H.-H, and Nielsen, A.S.: Full spectrum inversion of radio occultation signals, Radio Sci., 38(3), 1040, doi:10.1029/2002RS002763, 2003.

Johnston, B. R., Xie, F., and Liu, C.: The effects of deep convection on regional temperature structure in the tropical upper troposphere and lower stratosphere, J. Geophys. Res.: Atmos., 123, 1585−1603, doi.org/10.1002/2017JD027120, 2018.

Klein, S. A., and Hartmann, D. L.: The seasonal cycle of low stratiform clouds. Journal of Climate, 6, 1587−1606, doi:10.1175/1520-0442(1993)006<1587:TSCOLS>2.0.CO;2, 1993.

Kursinski, E. R., Hajj, G. A., Schofield, J. T., Linfield, R. P., and Hardy, K. R.: Observing Earth's atmosphere with radio occultation measurements using the Global Positioning System, J. Geophys. Res.: Atmos., 102, 23429−23465, doi.org/10.1029/97jd01569, 1997.

Kursinski, E. R., G. A. Hajj, Leroy, S. S., and Herman, B.: The GPS Radio Occultation Technique. Terr. Atmos. Ocean. Sci. (TAO), 11, 53−114, 2000.

Lewis, E. R.: Marine ARM GPCI Investigation of Clouds (MAGIC) Field Campaign Report. U.S. Department of Energy, https://doi.org/10.2172/1343577, 2016.

Maddy, E. S. and Barnet, C. D.: Vertical resolution estimates in version 5 of AIRS operational retrievals. IEEE Transactions on Geoscience and Remote Sensing, 46, 2375−2384, doi:10.1109/TGRS.2008.917498, 2008.

Nelson, K. J., Xie, F., Ao, C. O., and Oyola-Merced, M. I.: Diurnal Variation of the Planetary Boundary Layer Height Observed from GNSS Radio Occultation and Radiosonde Soundings over the Southern Great Plains. J. Atmos. Oceanic Tech., 38, 2081−2093, https://doi.org/10.1175/jtech-d-20-0196.1, 2021.

Nelson, K. J., Xie, F., Chan, B. C., Goel, A., Kosh, J., Reid, T. G. R., Snyder, C. R., and Tarantino, P. M.: GNSS Radio Occultation Soundings from Commercial Off-the-Shelf Receivers Onboard Balloon Platforms, Atmos. Meas. Tech., https://doi.org/10.5194/amt-2022-198, 2022.

Painemal, D., Minnis, P., and Nordeen, M.: Aerosol variability, synoptic-scale processes, and their link to the cloud microphysics over the northeast Pacific during MAGIC, J. Geophys. Res. Atmos., 120, 5122–5139, doi:10.1002/2015JD023175, 2015.

Patterson, W. L.: Climatology of Marine Atmospheric Refractive Effects: A Compendium of the Integrated Refractive Effects Prediction System (IREPS) Historical Summaries. Naval Ocean Systems Center, https://apps.dtic.mil/sti/pdfs/ADA155241.pdf, 1982.

Ramanathan, V., Cess, R. D., Harrison, E. F., Minnis, P., Barkstrom, B. R., Ahmad, E., and Hartmann, D.: Cloud-radiative forcing and climate: Results from the Earth Radiation Budget Experiment, Science, 243, 57–63, DOI:10.1126/science.243.4887.57, 1989.

Rocken, C., Anthes, R., Exner, M., Hunt, D., Sokolovskiy, S., Ware, R., Gorbunov, M., Schreiner, W., Feng D., Herman B., Kuo, Y.-H., Zou, X.: Analysis and validation of GPS/MET data in the neutral atmosphere. J. Geophys. Res., 102, 29849−29866, https://doi.org/10.1029/97JD02400, 1997.

Schreiner, W. S., Weiss, J.P., Anthes, R.A., Braun, J., Chu, V., Fong, J., Hunt, D., Kuo, Y.-H., Meehan, T., Serafino, W., Sjoberg, J., Sokolovskiy, C., Talaat, E., Wee, T.K., Zeng, Z.: COSMIC-2 Radio Occultation Constellation: First Results. Geophys. Res. Lett., 47, https://doi.org/10.1029/2019gl086841, 2020.

https://doi.org/10.5194/amt-2023-150
Preprint. Discussion started: 24 July 2023

Atmospheric Measurement Techniques Discussions

Seidel, D. J., Ao, C.O. and Li, K.: Estimating climatological planetary boundary layer heights from radiosonde observations: Comparison of methods and uncertainty analysis, J. Geophys. Res., 115, D16114, doi:10.1029/2009JD013680, 2010.

Smith, E. K. and Weintraub, S.: The Constants in the Equation for Atmospheric Refractivity Index at Radio Frequencies. Proc. IRE, 41, 1035−1037, doi:10.1109/JRPROC.1953.274297, 1953.

Sokolovskiy, S. V.: Modeling and Inverting Radio Occultation Signals in the Moist Troposphere. Radio Sci., 36, 441−458, https://doi.org/10.1029/1999RS002273, 2001.

Sokolovskiy, S. V.: Effect of super refraction on inversions of radio occultation signals in the lower troposphere. Radio Sci., 38 (3), https://doi.org/10.1029/2002RS002728, 2003.

Sokolovskiy, S. V., Kuo, Y.-H., Rocken, C., Schreiner, W. S., Hunt, D. and Anthes, R. A., 2006: Monitoring the atmospheric boundary layer by GPS radio occultation signals recorded in the open-loop mode. Geophys. Res. Lett., 33, L12813, doi:10.1029/2006GL025955, 2006.

Stull, R., Santoso, E., Berg, L. K., and Hacker, J.: Boundary Layer Experiment 1996 (BLX96), BAMS, 78, 1149−1158, doi: 10.1175/1520-0477(1997)078<1149:BLEB>2.0.CO;2, 1997.

Stull, R. B.: An Introduction to Boundary Layer Meteorology. Kluwer Academic Publishers, 666 pp., ISBN 90-277-2768-6, 1988.

von Engeln, A. and Teixeira, J.: A Planetary Boundary Layer Height Climatology Derived from ECMWF Reanalysis Data, J. Climate, 26, 6575−6590, https://doi.org/10.1175/jcli-d-12-00385.1, 2013.

Winning, T. E., Chen, Y.-L., and Xie, F.: Estimation of the marine boundary layer height over the central North Pacific using GPS radio occultation, Atmospheric Research, 183, 362−370, https://doi.org/10.1016/j.atmosres.2016.08.005, 2017.

Wood, R., Mechoso, C. R., Bretherton, C. S., Weller, R. A., Huebert, B., Straneo, F., Albrecht, B. A., Coe, H., Allen, G., Vaughan, G., Daum, P., Fairall, C., Chand, D., Gallardo Klenner, L., Garreaud, R., Grados, C., Covert, D. S., Bates, T. S., Krejci, R., Russell, L. M., de Szoeke, S., Brewer, A., Yuter, S. E., Springston, S. R., Chaigneau, A., Toniazzo, T., Minnis, P., Palikonda, R., Abel, S. J., Brown, W. O. J., Williams, S., Fochesatto, J., Brioude, J., and Bower, K. N.: The VAMOS Ocean-Cloud-Atmosphere-Land Study Regional Experiment (VOCALS-REx): goals, platforms, and field operations, Atmos. Chem. Phys., 11, 627−654, https://doi.org/10.5194/acp-11-627-2011, 2011.

https://doi.org/10.5194/amt-2023-150
Preprint. Discussion started: 24 July 2023

Xie, F., Syndergaard, S., Kursinski, E. R., and Herman, B.M.: An Approach for Retrieving Marine Boundary Layer Refractivity from GPS Occultation Data in the Presence of Super-refraction. J. Atmos. Oceanic Technol., 23, 1629−1644, https://doi.org/10.1175/JTECH1996.1, 2006.

Xie, F., Haase, J. S., and Syndergaard, S.: Profiling the Atmosphere Using the Airborne GPS Radio Occultation Technique: A Sensitivity Study. IEEE Transactions on Geoscience and Remote Sensing, 46, 3424−3435, https://doi.org/10.1109/tgrs.2008.2004713, 2008.

Xie, F., Wu, D. L., Ao, C. O., Kursinski, E. R., Mannucci, A. J., and Syndergaard, S.: Super-refraction effects on GPS radio occultation refractivity in marine boundary layers, Geophys. Res. Lett., 37, https://doi.org/10.1029/2010gl043299, 2010.

Xie, F., Wu, D. L., Ao, C. O., Mannucci, A. J., and Kursinski, E. R.: Advances and limitations of atmospheric boundary layer observations with GPS occultation over southeast Pacific Ocean, Atmos. Chem. Phys., 12, 903−918, doi:10.5194/acp-12-903-2012, 2012.

Zhou, X., Kollias, P., and Lewis, E.: Clouds, precipitation and marine boundary layer structure during MAGIC. J. Climate, 28, 2420−2442, https://doi.org/10.1175/JCLI-D-14-00320.1, 2015.